J. Fluid Mech. (2020), *vol.* 888, A23. © The Author(s), 2020.
Published by Cambridge University Press
doi:10.1017/jfm.2020.64

Optimal configuration of a two-dimensional bristled wing

Seung Hun Lee[1], **Minhyeong Lee**[1] **and Daegyoum Kim**[1,†]

[1]Department of Mechanical Engineering, KAIST, Daejeon 34141, Republic of Korea

(Received 19 June 2019; revised 23 December 2019; accepted 15 January 2020)

In contrast to common continuous wings, microscopic flying insects such as fairyfly and thrips possess extraordinary wings that comprise several bristles. In the low-Reynolds-number environment inhabited by these insects, a bristled wing benefits from the formation of virtual fluid barriers that prevent flow leakage in the gaps of bristles. In this study, the optimal configuration regarding the aerodynamic performance of simple bristled-wing models is investigated numerically in terms of the Reynolds number and the distance between bristles, which are known to be important parameters for determining the effectiveness of a virtual fluid barrier. Inspired by the inherent characteristics of low-Reynolds-number flow, we provide new insights into the aerodynamics of a bristled wing by using a scaling parameter that combines these two independent parameters: effective gap width. In addition, the force ratio is scaled with the Reynolds number to better characterize the generation of drag and lift by a bristled wing. Despite the Reynolds number and the gap width varying by several orders of magnitude, the scaled drag force converges asymptotically beyond a specific effective gap width, and the lift force ratio has a peak within a very narrow range of the effective gap width. The trend of the lift with the effective gap width is correlated with changes in the asymmetric distributions of pressure and vorticity on the surface of the bristles. In addition, the drag and lift predicted theoretically, by invoking the linear superposition of creeping flows, agree well with numerical results, in particular for large effective gap width.

Key words: swimming/flying

1. Introduction

Because flying insects exhibit exceptional manoeuvrability and flight performance, the kinematic and morphological features of their wings and the physical principles of their flight capabilities have been of interest in biofluid mechanics and bio-inspired engineering. Most previous studies of insect flight have investigated continuous wings with no discontinuities due to gaps on the wing surfaces (e.g. Weis-Fogh 1973; Ellington *et al.* 1996; Dickinson, Lehmann & Sane 1999). However, microscopic flying insects such as the fairyfly (Mymaridae) and thrips (Thysanoptera), which inhabit the low-Reynolds-number flow regime, have evolved bristled wings that

† Email address for correspondence: daegyoum@kaist.ac.kr

https://doi.org/10.1017/jfm.2020.64 Published online by Cambridge University Press

comprise a main frame and several cylindrical bristles that extend from the main frame with gaps between them. For images of bristled wings, see George & Huber (2011), Huber & Noyes (2013) and Lee, Lahooti & Kim (2018).

Microscopic hairy structures are common on the appendages of small organisms (Koehl 1996; Koehl *et al.* 2001). With decreasing Reynolds number, viscous flow around an array of hairs undergoes a notable transition so that the array changes its function from a sieve to a paddle (Umemura 1982; Lee & Leal 1986; Cheer & Koehl 1987). Vorticity generated on a solid surface is confined to a thin shear layer in the high-Reynolds-number flow, and the effect of viscous diffusion is not critical for aerodynamic interaction of multiple lift-generating bodies closely arranged (Kim, Lee & Kim 2019). However, for the low-Reynolds-number flow of relatively slow surrounding fluid and narrow gaps, vorticity of the shear layers developed from the solid surface is diffused strongly away from the surface, and the diffused shear layers eventually form virtual fluid barriers in the gaps between the bodies (Nawroth *et al.* 2010). This reduces the leakage through the gaps appreciably, thereby changing how the array functions. That is, discrete solid objects of the array behave as if they were aerodynamically continuous, and mutual aerodynamic interaction by strong viscous diffusion is of great importance for the array. With this principle, micro-aerodynamic decelerators made of multiple nanofibre mats were proposed by Zussman, Yarin & Weihs (2002) for potential applications as passive airborne platforms. In addition, it was reported recently that the porosity of the dandelion pappus tunes precisely to stabilize the vortical structure formed behind during wind dispersion, which can maximize aerodynamic loading while minimizing material requirements (Cummins *et al.* 2018).

The fairyfly and thrips also use virtual fluid barriers between their bristles for aerial flight. An experimental study with a scaled-up translating or rotating bristled wing reported that such a wing generated slightly lower aerodynamic force compared to that of a smooth wing with no gaps (Sunada *et al.* 2002). Subsequently, the aerodynamic advantages of bristled wings were studied analytically (Barta & Weihs 2006; Weihs & Barta 2008) and numerically (Davidi & Weihs 2012). The virtual fluid barriers compensate for the reduced force due to the gaps and allow a bristled wing to have a higher force coefficient; here, the actual surface area is considered when defining the force coefficient. Recently, Lee & Kim (2017) studied the flow structure of a three-dimensional (3-D) translating bristled-wing model experimentally. They identified the Reynolds-number-dependent behaviour of the shear layers in the gaps between the bristles and how that affects the formation of leading-edge vortices and the generation of lift.

Besides simple translating motion, more complicated motion and the kinematic patterns of actual wings have been investigated. Barta (2011) examined theoretically a row of oscillating slender bodies in Stokes flow and presented parametric results with respect to the oscillation frequency, the number of bristles, the slenderness ratio and the space between bristles. Recently, Lee *et al.* (2018) investigated the vortices generated within the gaps of a flapping bristled wing, with particular emphasis on the phase of stroke reversal; they showed that the flow in the gaps responds faster to wing motion as the Reynolds number decreases. Santhanakrishnan *et al.* (2014) modelled a bristled wing as a porous membrane wing and showed that in wing–wing interaction through the clap-and-fling mechanism, flow leakage through the wing surfaces reduces the drag required to fling the wings apart; a pair of porous wings can therefore achieve a large lift-to-drag ratio over a flapping cycle. This study was extended to a numerical simulation of a two-dimensional (2-D) bristled wing (Jones *et al.* 2016) and an experimental study of a 3-D bristled wing (Kasoju *et al.* 2018).

https://doi.org/10.1017/jfm.2020.64 Published online by Cambridge University Press

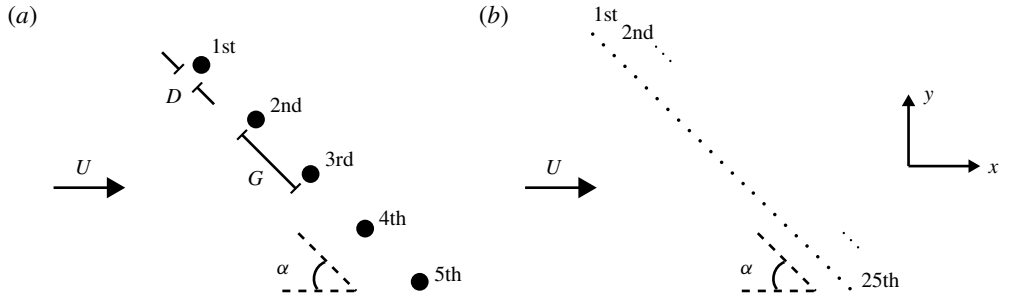


FIGURE 1. Schematic diagrams of (*a*) five-bristle model and (*b*) 25-bristle model.

While previous studies have considered the Reynolds number and the gap width as the main independent parameters regarding the aerodynamic effects of gaps, the underlying principles of optimizing the configuration of a bristled wing to enhance its aerodynamic force remain unclear despite their importance in bio-inspired applications. In the present study, as the first step in a new approach to analysing aerodynamic force generation and revealing the combined effects of the dynamic and kinematic parameters (i.e. Reynolds number and gap width), we investigate numerically how the aerodynamic force and flow structure of a 2-D bristled wing fixed in space vary over wide ranges of the Reynolds number and gap width. Unlike an infinite-Reynolds-number solution, where the aerodynamics are characterized by the diameter of each bristle, the aerodynamics in the low-Reynolds-number regime depend on the gap width because the viscous diffusion across the gap between the bristles is of great importance. That is, the Reynolds number based on the gap width is a governing parameter in the low-Reynolds-number regime. With this in mind, we propose new insights into the characteristics of the drag and lift acting on each bristle and the entire wing. We then compare the aerodynamic forces predicted by a simple but reliable theoretical model with those obtained by numerical simulations to assess whether our approach is effective for finding the optimal configuration.

2. Problem description

2.1. *Bristled-wing model*

We introduce simplified 2-D bristled-wing models that capture the features of a biological bristled wing as used by Jones *et al.* (2016) and Lee *et al.* (2018). As a preliminary exploration of the effects of the Reynolds number and the gap size, we begin by considering a simple five-bristle model, which consists of five equally spaced cylinders (bristles) of identical diameter D, aligned in a straight line (figure 1*a*). Admittedly, the number of bristles is smaller than that of the actual bristled wing found in nature. To confirm whether the main findings from the five-bristle model can be generalized, we also examine a 25-bristle model with 25 equally spaced bristles of equal diameter D in a straight line (figure 1*b*).

We define the gap width G as the distance between the centres of two adjacent bristles. The Reynolds number Re_D $(=\rho UD/\mu)$ based on the bristle diameter ranges between 0.01 and 1.0, i.e. $Re_D = [0.01, 0.02, 0.05, 0.1, 0.2, 0.5, 1.0]$; here, U is the free-stream velocity, ρ is the fluid density and ν $(=\mu/\rho)$ is the fluid kinematic viscosity. For both five-bristle and 25-bristle models, the normalized gap width between two adjacent bristles is $G/D = 3$–2000. By the definitions of G and D (figure 1*a*), $G/D = 1$

https://doi.org/10.1017/jfm.2020.64 Published online by Cambridge University Press

Re_D	0.01	0.02	0.05	0.1	0.2	0.5	1.0
Khalili & Liu (2017)	371.4	206.3	96.6	55.3	32.3	16.5	10.3
Present work	375.6	209.3	97.9	56.1	32.8	16.7	10.4

TABLE 1. Comparison of drag coefficients ($C_d = 2F/\rho U^2 D$) for a circular cylinder in a uniform free stream.

means the bristles are in contact. The large variations in the orders of Re_D and G/D are intended to find the optimal configuration of the model regarding lift generation.

For both models, we define an angle of attack α as the angle between the straight line connecting the bristles and the x axis parallel to the direction of the free stream (figure 1). For the five-bristle model, α varies from 15° to 90°, i.e. $\alpha = [15°, 30°, 45°, 60°, 70°, 90°]$ (figure 1*a*). For the 25-bristle model, α is fixed to be 45° (figure 1*b*).

2.2. *Numerical method*

The 2-D incompressible laminar flow around a bristle model is solved numerically using OpenFOAM. We use the simpleFoam solver for steady-state solutions and the second-order Gauss-linear scheme for spatial discretizations, and we set the time derivative as zero for steady-state solutions in low-Reynolds-number flow. Although the kinematics of an actual wing are unsteady, in this study, we focus on revealing the steady aerodynamic performance of the model and thus consider steady-state solutions.

For our numerical simulations, we construct the rectangular fluid domain $[-2.5 \times 10^5 D, 2.5 \times 10^5 D] \times [-2.5 \times 10^5 D, 2.5 \times 10^5 D]$ and 10 layers of structured grids near each bristle. The grid size next to a bristle is fixed as $0.01D$. Outside the structured layers, we construct triangular grids of exponentially increasing size with the growth ratio of 1.05 for the rectangular region that encompasses all the bristles; the size of this region depends on the gap size or the number of bristles. Finally, we construct structured grids of exponentially increasing size with the growth ratio of 1.05 for the rest of the fluid domain. The total number of cells is less than 1.0×10^6 for the 25-bristle model and varies slightly depending on the gap size and the number of bristles. To check grid convergence, we change the minimum size of the grid from $0.01D$ to $0.02D$ while keeping all other conditions the same. At $Re_D = 0.1$, the values of the drag coefficient $C_d = 2F/\rho U^2 D$ for a circular cylinder in a uniform free stream derived from the fine-grid and coarse-grid cases differ little, being $C_d = 56.1$ and 56.0, respectively. This result justifies our decision to use $0.01D$ as the minimum grid size.

For validation of our numerical method, we conduct numerical simulations to obtain the values of the drag coefficient C_d for a circular cylinder in a uniform free stream for Re_D ranging between 0.01 and 1.0. Table 1 compares our results with numerical results by Khalili & Liu (2017) and shows that our results are consistent with their results for $Re_D \leqq 1$.

3. Results and discussion

3.1. *Aerodynamic characteristics of five-bristle model*

We first begin by considering the five-bristle model at $\alpha = 90°$ (figure 1*a*) to determine how the gap size G/D and the Reynolds number Re_D affect the aerodynamic

https://doi.org/10.1017/jfm.2020.64 Published online by Cambridge University Press

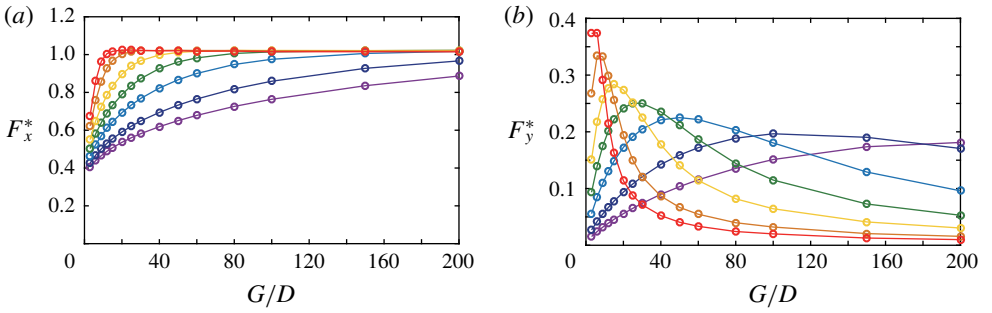


FIGURE 2. (*a*) Drag force and (*b*) lift force of the uppermost (first) bristle in the five-bristle model at $\alpha = 90°$ for $Re_D = 1$ (red), 0.2 (orange), 0.5 (yellow), 0.1 (green), 0.05 (blue), 0.02 (navy) and 0.01 (purple). Note that the vertical range differs between panels (*a*) and (*b*).

forces and corresponding flow structures. We then extend the main findings for the five-bristle model at $\alpha = 90°$ to the five-bristle model with other angles of attack, and furthermore to the 25-bristle model. The x-directional force F_x (drag) and the y-directional force F_y (lift) acting on the first uppermost bristle are normalized by the drag force $F_{x,s}$ of a single isolated bristle obtained at the same Re_D:

$$F_x^* = F_x/F_{x,s} \quad \text{and} \quad F_y^* = F_y/F_{x,s}. \tag{3.1a,b}$$

Note that F_y is normalized by $F_{x,s}$ because the lift $F_{y,s}$ of the single isolated bristle is zero. The normalized drag F_x^* and lift F_y^* of the first bristle in the five-bristle model at $\alpha = 90°$ are provided for $Re_D = 0.01$–1 in figure 2. Because the flow is symmetric with respect to the third bristle for low-Reynolds-number flow, we show the forces for the first bristle only. Although the forces on the second bristle are not presented, they follow similar trends to the first bristle, with minor differences in their magnitudes (see figure 7*a*,*b* later). For the first bristle F_x^* approaches that of the single bristle asymptotically as either Re_D or G/D increases (figure 2*a*). The F_x^* value converges to unity at smaller G/D for higher Re_D. For instance, for $Re_D = 1$, F_x^* reaches unity at $G/D < 20$, whereas for $Re_D = 0.01$, it remains below 0.9 even at $G/D > 200$.

At $\alpha = 90°$, the first and second bristles experience lifts that are equal in magnitude and opposite in sign to the fifth and fourth bristles, respectively: positive lifts for the first and second bristles, and negative lifts for the fourth and fifth bristles. Note that no lift is found for the third bristle because of the symmetry of flow. For given Re_D, F_y^* of the first bristle tends to increase and then decrease with G/D, thereby having a peak (figure 2*b*). After the peak, F_y^* asymptotes to zero as G/D goes to infinity. The maximum F_y^* occurs at smaller G/D for higher Re_D. Compare $Re_D = 0.2$ and $Re_D = 0.02$ in figure 2(*b*), for which the values of G/D corresponding to maximum lift are approximately 15 and 100, respectively.

To correlate the aforementioned force variation with the flow structure, we examine the force distributions on the surface of the first bristle as well as the pressure and vorticity fields around it (figures 3 and 4). We decompose the force $\boldsymbol{F}$ exerted on a bristle into two components, force due to pressure and force due to viscous stress, i.e.

$$\boldsymbol{F} = \int_S -p\boldsymbol{n}\,\mathrm{d}S + \int_S \boldsymbol{n}\cdot\boldsymbol{\tau}\,\mathrm{d}S, \tag{3.2}$$

https://doi.org/10.1017/jfm.2020.64 Published online by Cambridge University Press

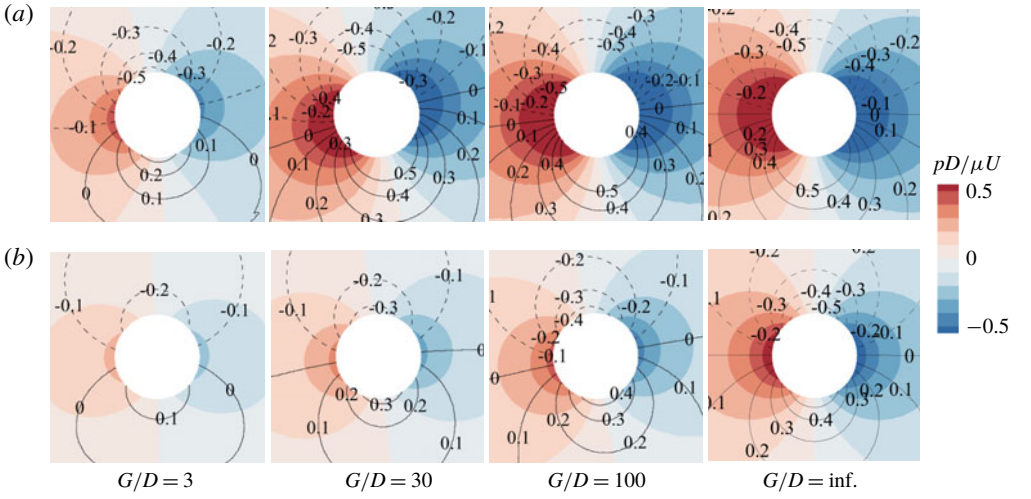


FIGURE 3. Pressure and vorticity contours around the first bristle of the five-bristle model at $\alpha = 90°$ for $Re_D = 0.1$ (*a*) and 0.01 (*b*). The dashed and solid contour lines denote negative and positive vorticities ($\omega D/U$), respectively, and $G/D = \text{inf.}$ indicates the case of a single isolated cylinder.

where $\boldsymbol{n}$ is the unit normal vector into the fluid domain, p is the pressure, $\boldsymbol{\tau}$ is the viscous stress tensor and S is the surface of the bristle. Note that the viscous stress tensor on the surface is related to the vorticity thereon as $\boldsymbol{n} \cdot \boldsymbol{\tau} = -\mu \boldsymbol{n} \times \boldsymbol{\omega}$, which is why we examine the vorticity field in figure 3. Both the pressure force $-p\boldsymbol{n}$ per unit surface area and the viscous force $\boldsymbol{n} \cdot \boldsymbol{\tau}$ per unit surface area are non-dimensionalized by D, μ and U, respectively: $-p\boldsymbol{n}D/\mu U$ and $\boldsymbol{n} \cdot \boldsymbol{\tau} D/\mu U$. To examine how they contribute to the x- and y-directional forces, we denote $f_{p,x}$ and $f_{p,y}$ as the x- and y-directional components of $-p\boldsymbol{n}D/\mu U$, respectively. Likewise, we denote $f_{v,x}$ and $f_{v,y}$ as the x- and y-directional components of $\boldsymbol{n} \cdot \boldsymbol{\tau} D/\mu U$, respectively. Because in creeping flow the viscous and pressure forces are comparable, these two force components should be considered together.

We begin with the smallest gap $G/D = 3$, for which F_x^* is reduced significantly; e.g. $F_x^* = 0.50$ at $Re_D = 0.1$ and $F_x^* = 0.41$ at $Re_D = 0.01$ (figure 2). For $Re_D = 0.1$ and 0.01, both the pressure and the vorticity around the bristles become considerably weaker than those of a single isolated bristle ($G/D = \text{inf.}$), thereby reducing the magnitudes of the drag components $f_{p,x}$ and $f_{v,x}$ (figures 3 and 4). Interestingly, the x component $f_{v,x}$ of the viscous force is reduced more notably on the lower surface of the bristle ($\theta = 180°$–$360°$). For $G/D = 3$ and $Re_D = 0.1$, the maximum values of $f_{v,x}$ on the upper and lower surfaces are 0.56 and 0.35, respectively. Meanwhile, the x component $f_{p,x}$ of the pressure force is reduced almost equally on the windward and leeward surfaces (figure 4*a*,*b*). An asymmetrically distributed viscous force and a symmetrically distributed pressure force are also found for the y components $f_{p,y}$ and $f_{v,y}$ (figure 4*c*,*d*). Similar trends at $G/D = 3$ and $Re_D = 0.01$ are found for all of the force components (figure 4*e*–*h*).

As the gap increases beyond $G/D = 3$, the pressure gradient and vorticity around the bristle become stronger (figure 3), and correspondingly the magnitudes of the surface forces grow gradually and approach those of the single isolated bristle (figure 4). The difference in $f_{v,x}$ between the upper and lower surfaces of the bristle diminishes with

https://doi.org/10.1017/jfm.2020.64 Published online by Cambridge University Press

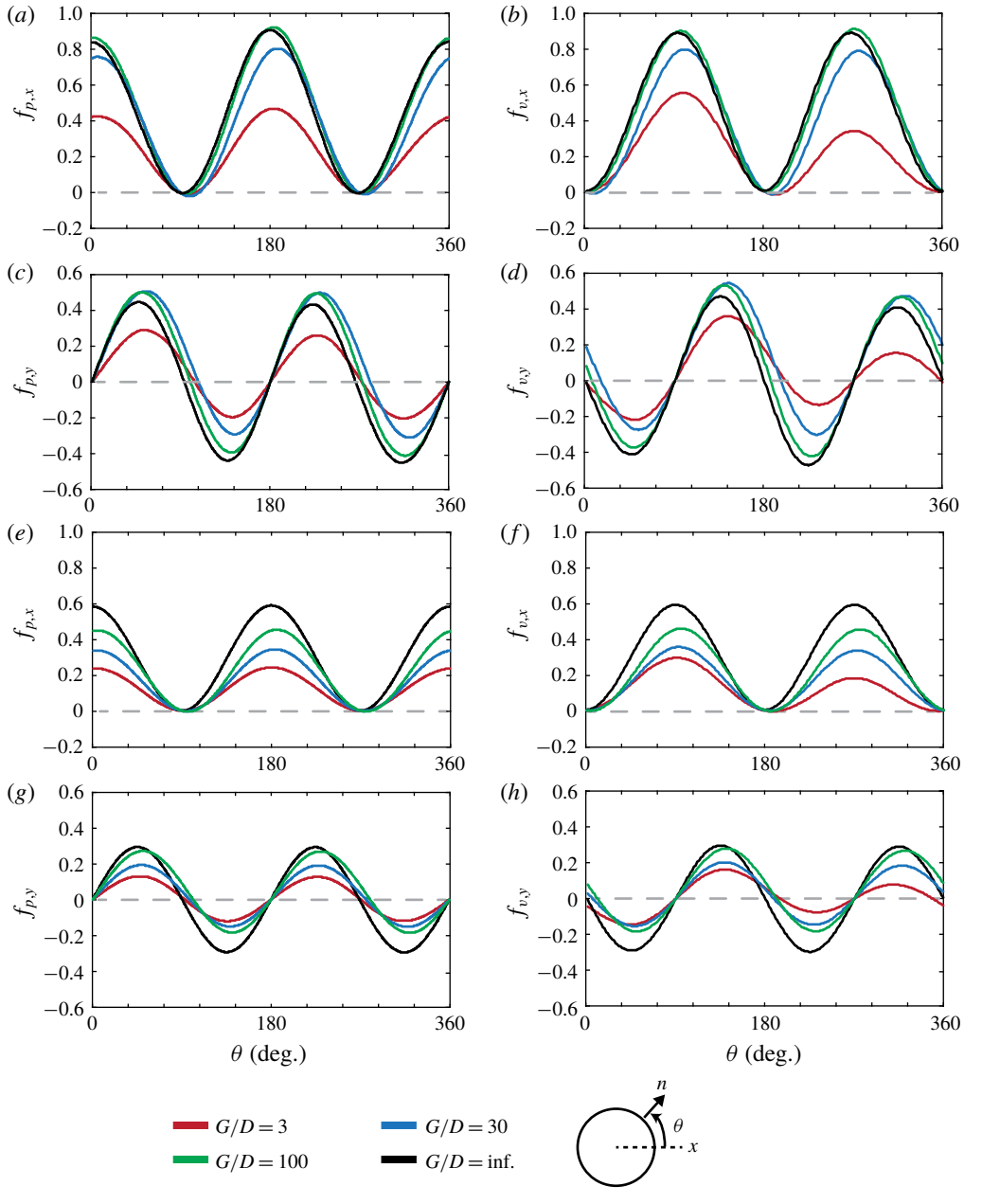


FIGURE 4. Spatial distributions of forces due to pressure and viscous stress per unit surface area acting on the surface of the first bristle in the five-bristle model at $\alpha = 90°$ for (*a–d*) $Re_D = 0.1$ and (*e–h*) $Re_D = 0.01$.

G/D (figure 4*b*,*f*). Similarly, the difference in $f_{v,y}$ between the windward and leeward surfaces reduces with G/D (figure 4*d*,*h*). Even for the large gap width of $G/D = 100$, however, significant deviations between the curves for $G/D = 100$ and $G/D = \text{inf.}$ are still noted at $Re_D = 0.01$ (figure 4*e–h*). This implies that, even if the bristles are separated by the same distance, they are more aerodynamically coupled when the

https://doi.org/10.1017/jfm.2020.64 Published online by Cambridge University Press

Reynolds number is smaller; e.g., for $G/D = 100$, $F_x^* = 1.0$ at $Re_D = 0.1$ and $F_x^* = 0.76$ at $Re_D = 0.01$ (figure 2).

Another notable feature of the flow structure is that the incident flow is deflected in such a way that the bristles repel each other. The incoming flow is deflected upwards for the upper (first and second) bristles and downwards for the lower (fourth and fifth) bristles. Accordingly, the pressure and vorticity fields around the upper bristles are tilted slightly in the anticlockwise direction, thereby generating lift (figure 3). To quantify how much the flow field is tilted compared to that of the single isolated cylinder, we draw a line connecting the two points on the bristle surface where the vorticity is zero and define the tilting angle θ_t as the angle between this line and the x axis. For θ_t, we could alternatively take the angle between the x axis and the line connecting the two points on the bristle surface at which the pressure is maximum or minimum. The tilting angles computed by these two definitions differ slightly, and hereinafter we use the former definition involving the line connecting the points of zero vorticity.

The tilting angle θ_t is closely related with the lift force; this correlation is observed no matter which definition of θ_t is used. For $Re_D = 0.1$, the tilting angle is greatest at $G/D = 30$, at which value the lift is greatest (figure 2*b*): we have $\theta_t = 10^\circ$ at $G/D = 3$, $\theta_t = 16^\circ$ at $G/D = 30$ and $\theta_t = 6^\circ$ at $G/D = 100$. Because of the tilting, the negative peaks of $f_{p,y}$ and $f_{v,y}$ are roughly 65 %–70 % of those of the single isolated bristle at $G/D = 30$, while the corresponding positive peaks are similar to those of the single isolated bristle (figure 4*c*,*d*). For much larger gap size, namely $G/D = 100$, which exhibits less tilting, the positive peaks of $f_{p,y}$ and $f_{v,y}$ do not change from those of $G/D = 30$. Meanwhile, the negative peaks approach those of the single bristle, thereby reducing the lift.

3.2. *Effective gap width of five-bristle model*

3.2.1. *Five-bristle model at* $\alpha = 90^\circ$

In § 3.1, we showed that the forces exerted on a bristle depend strongly on both G/D and Re_D. In fact, there have been previous studies of the aerodynamic interaction of multiple bodies caused by strong viscous effects, although they did not discuss in detail how the pressure and viscous surface forces vary with gap width and Reynolds number (Barta & Weihs 2006; Lee *et al.* 2018). In those previous studies, Re_D and G/D were treated independently. However, based on our results in § 3.1, we conjecture that the two parameters are coupled aerodynamically in that increasing G/D has the same effect as increasing Re_D in terms of force generation (figure 2).

To evaluate the combined effects of G/D and Re_D, we begin by examining the Reynolds-number-dependent spatial scale of 2-D creeping flow around a single isolated bristle (cylinder). Analytical approximations exist for flow around a cylinder at Reynolds numbers less than unity. For example, Proudman & Pearson (1957) used the method of matched asymptotic expansions to match the inner Stokes solution to the outer Oseen solution, and *vice versa*. In the Stokes solution, a convective term in the governing equation is neglected, while the Oseen solution considers a linearized convective term in the governing equation. According to Proudman & Pearson (1957), the Oseen solution for the streamfunction ψ over a cylinder in polar coordinates is the expansion

$$\psi = \psi_0(r^* Re_D, \theta) + F_1(Re_D)\psi_1(r^* Re_D, \theta) + F_2(Re_D)\psi_2(r^* Re_D, \theta) + \cdots, \tag{3.3}$$

where $Re_D = UD/\nu$ and r^* is the dimensionless radial coordinate normalized by the cylinder radius: $r^* = r/R = 2r/D$. The term $F_{n+1}(Re_D)/F_n(Re_D)$ vanishes as Re_D

https://doi.org/10.1017/jfm.2020.64 Published online by Cambridge University Press

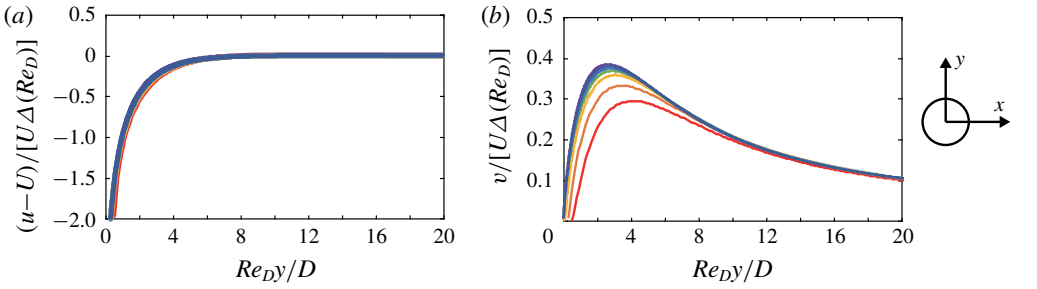


FIGURE 5. Profiles of (*a*) *x*-directional and (*b*) *y*-directional velocity disturbances around a single isolated bristle on positive *y* axis, which are normalized by the free-stream velocity U and $\Delta(Re_D) = (\ln(8/Re_D) - \gamma + 0.5)^{-1}$. The scaled distance $Re_D\, y/D$ is used instead of y/D. The plots are for $Re_D = 1$ (red), 0.2 (orange), 0.5 (yellow), 0.1 (green), 0.05 (blue), 0.02 (navy) and 0.01 (purple).

approaches zero, making the higher-order terms negligible. For the Oseen expansion in (3.3), we use the Oseen variable $\hat{r} = r^* Re_D$ so that the radial coordinate r is scaled by the viscous dimension ν/U, i.e. $\hat{r} = 2rU/\nu$. This expansion matches the Stokes region of the flow asymptotically at $r^* = O(1)$. Van Dyke (1975) showed that, for small $\hat{r}$, the Oseen expansion can be approximated as

$$\psi \approx \frac{UR}{Re_D}\left[\hat{r}\sin\theta + \Delta(Re_D)\left\{\left(\ln\frac{\hat{r}}{8} + \gamma - 1\right)\hat{r}\sin\theta + O(\hat{r}^2\ln\hat{r}) + \cdots\right\} + \cdots\right], \tag{3.4}$$

where $\gamma = 0.5772$ is Euler's constant and $\Delta(Re_D) = (\ln(8/Re_D) - \gamma + 0.5)^{-1}$. See also Proudman & Pearson (1957) and Van Dyke (1975) for detailed procedures for the solution of the creeping flow around a cylinder. The first term on the right-hand side of (3.4) represents the uniform free stream, and the second term describes the disturbance fields produced by the cylinder when the higher-order terms are neglected. Its Reynolds-number-dependent constant $\Delta(Re_D)$ decreases with Re_D, thereby reducing the magnitude of disturbances. As well as the streamfunction disturbance, the velocity disturbance should depend on $\hat{r}$ $(= r^* Re_D)$, i.e. $u_r = \partial\psi/r\partial\theta$ and $u_\theta = -\partial\psi/\partial r$. That is, regarding the velocity disturbance, Re_D^{-1} is an appropriate characteristic scale for the dimensionless length r^* of the creeping flow around the bristle (Van Dyke 1975).

As given by our numerical simulation, the profiles of the velocity disturbance caused by a single isolated bristle on the positive y axis are depicted in figure 5. Because we have the Reynolds-number-dependent constant $\Delta(Re_D)$ in the second term of (3.4), the velocity disturbances $u - U$ and v are normalized by $\Delta(Re_D)$ as well as the free-steam velocity U in figure 5: $(u - U)/[U\Delta(Re_D)]$ and $v/[U\Delta(Re_D)]$. Also, y/D is divided by Re_D^{-1} to introduce a new scaled y coordinate $Re_D\, y/D$ in figure 5.

The velocity profiles in figure 5 are determined by the scaled distance $Re_D\, y/D$ regardless of the Reynolds number. Although the Reynolds numbers considered in figure 5 differ by two orders of magnitude, i.e. $Re_D = 0.01$–1, the curves of the normalized x-velocity disturbance $(u - U)/[U\Delta(Re_D)]$ collapse onto a single curve: thus $(u - U)/[U\Delta(Re_D)]$ converges to zero near $Re_D\, y/D \approx 6$; and u becomes similar to U. The curves of the normalized y-velocity disturbance $v/[U\Delta(Re_D)]$ have similar shapes but show notable deviation at low $Re_D\, y/D$, in particular for the curves of

https://doi.org/10.1017/jfm.2020.64 Published online by Cambridge University Press

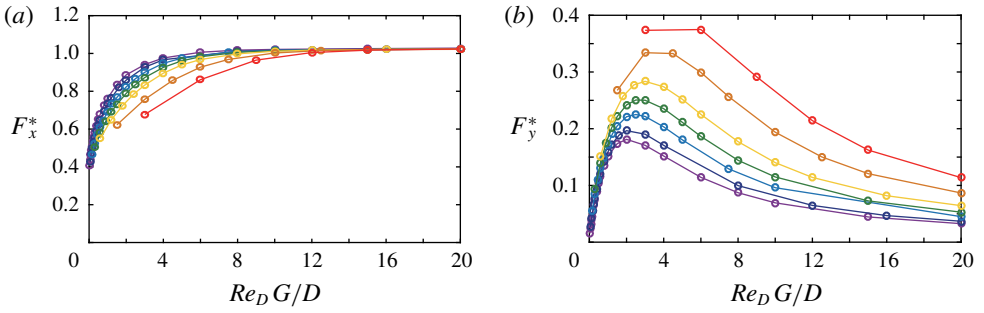


FIGURE 6. Figure 2 replotted with effective gap width $Re_D\,G/D$. The colours of the curves are those used in figure 2, namely $Re_D = 1$ (red), 0.2 (orange), 0.5 (yellow), 0.1 (green), 0.05 (blue), 0.02 (navy) and 0.01 (purple).

relatively large Re_D. Despite such deviation, the peaks of the $v/[U\Delta(Re_D)]$ curves appear in a very narrow range of $Re_D\,y/D$, between 2.6 for $Re_D = 0.01$ and 4.3 for $Re_D = 1.0$.

Given the linearity of creeping flow, the spatial scale of the flow around each bristle in the five-bristle model may be the same as that for the single isolated bristle. Furthermore, given that the velocity profile is characterized by $Re_D\,y/D$, the lift and drag forces F_x^* and F_y^* acting on each bristle may be predicted similarly by the scaled gap width $Re_D\,G/D$. Figure 2 is replotted as figure 6 with the scaled gap width $Re_D\,G/D$ instead of G/D. For different values of Re_D between 0.01 and 1, the curves of F_x^* show a consistent pattern and reside in the narrow range of 0.85–1.0 for $Re_D\,G/D \geqslant 6$. More interestingly, all the curves of F_y^* exhibit a peak at $Re_D\,G/D \approx 3$. Figure 6 shows that how the forces vary is determined by a single parameter $Re_D\,G/D$ that combines the effects of the Reynolds number and the gap size for low-Reynolds-number flow. In fact, $Re_D\,G/D$ is equal to the Reynolds number Re_G $(= UG/\nu)$ based on the gap width G as the characteristic length. However, to emphasize the combined effect of the two representative variables Re_D and G/D, we use $Re_D\,G/D$ rather than Re_G in this study and name it 'effective gap width'.

The aforementioned results offer insight into elucidating a clear difference between two asymptotic solutions: the very-low-Reynolds-number solution in which the array of bristles is impervious, and the infinite-Reynolds-number solution in which the bristles are aerodynamically independent of each other unless they are very close to each other. Aerodynamic performance is characterized by the diameter D of each bristle, i.e. Re_D, at the high Reynolds number of $Re_D \gg 1$. However, at the low Reynolds number of $Re_D \leqslant 1$, viscous diffusion across the gap between the bristles is of great importance, and thus aerodynamic performance is determined by the gap width G between the bristles, i.e. Re_G $(= Re_D\,G/D)$ rather than the bristle diameter D. As the Reynolds number decreases below $Re_D = 1$, the flow field converges asymptotically, and aerodynamic characterization by the effective gap width $Re_D\,G/D$ should be better suited. Indeed, in figures 5 and 6, with decreasing Re_D, the curves tend to collapse towards the asymptotic solution of very low Reynolds number. The streamwise velocity component converges to the asymptotic solution faster than the cross-flow velocity component (figure 5). Similarly, the drag strongly affected by the streamwise velocity component converges faster than the lift relevant to the cross-flow velocity component (figure 6).

https://doi.org/10.1017/jfm.2020.64 Published online by Cambridge University Press

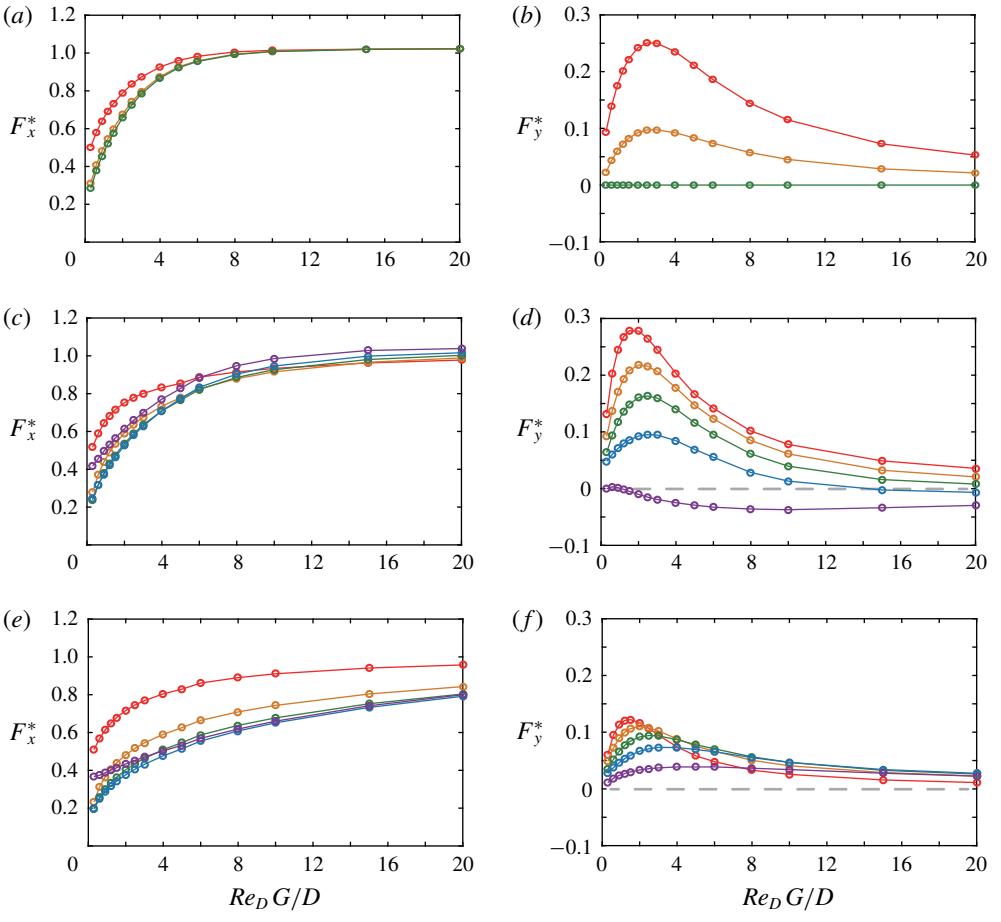


FIGURE 7. Drag and lift forces for individual bristles in the five-bristle model for $Re_D = 0.1$: (*a*,*b*) $\alpha = 90°$; (*c*,*d*) $\alpha = 45°$; and (*e*,*f*) $\alpha = 15°$. First bristle (red), second bristle (orange), third bristle (green), fourth bristle (blue) and fifth bristle (purple).

3.2.2. *Five-bristle model at* $\alpha < 90°$

Based on our analysis of the five-bristle model at $\alpha = 90°$, here we further consider the five-bristle model with various angles of attack (figure 1*a*), to confirm whether the performance of the five-bristle model can be characterized by the effective gap width $Re_D\,G/D$ for a wide range of the angle of attack. First, the lift and drag trends of each bristle are examined for three angles of attack, $\alpha = 90°$, 45° and 15°, and the Reynolds number $Re_D = 0.1$ as representative cases (figure 7). Note that data for $\alpha = 90°$ examined in § 3.2.1 are included in figure 7 for comparison. Although not presented here, we found that the overall trends were not altered notably by the change in the Reynolds number for the entire range of α and accordingly chose a single Reynolds number $Re_D = 0.1$ for figure 7. For $\alpha = 90°$, the forces exerted on each bristle depend on its relative position within the wing. As we mentioned in § 3.1, a bristle near the outer edge of the wing experiences greater drag and lift than do the inner bristles near the centre of the wing because the incoming flow decelerates in front of the inner bristles due to the formation of a virtual fluid barrier with the gaps (Lee *et al.* 2018). In our simulations for $Re_D = 0.1$, the values of F_x^* for the first and

https://doi.org/10.1017/jfm.2020.64 Published online by Cambridge University Press

second bristles are 0.87 and 0.80, respectively, at $Re_D\,G/D = 3.0$. For the same Re_D and $Re_D\,G/D$, the values of F_y^* for the first and second bristles are 0.25 and 0.097, respectively (figure 7*a*,*b*). Because of the symmetric flow, the curves for the fourth and fifth bristles are not included in figure 7(*a*,*b*).

For $\alpha = 45°$, in contrast to $\alpha = 90°$, the drag of the first bristle that faces the free stream head-on is larger than that of the fifth bristle at the trailing edge up to $Re_D\,G/D \approx 6$ (figure 7*c*). In the range of $Re_D\,G/D$, the drag force of the first bristle is greatest among the five. For example, for $Re_D\,G/D = 0.3$, the values of F_x^* for the first and fifth bristles are 0.52 and 0.42, respectively. The values of F_x^* for the remaining bristles lie in the range 0.24–0.28, much smaller than for the outermost bristles. As $Re_D\,G/D$ increases, the difference in F_x^* among all bristles decreases, and F_x^* approaches unity around $Re_D\,G/D = 20.0$. By contrast, F_y^* decreases sequentially from the first to the fifth bristle in the entire range of $Re_D\,G/D$, and even the fifth bristle produces negative lift in the entire range (figure 7*d*). Interestingly, except for the fifth bristle, each bristle has a peak in F_y^* in the narrow range of $Re_D\,G/D =$ 2.0–2.5. The value of $Re_D\,G/D$ that maximizes F_y^* increases slightly from the first to the fourth bristle.

At the lower angle of attack ($\alpha = 15°$), the drag force of the first bristle at the leading edge is dominant because it encounters the free stream directly whereas the other four bristles are not fully exposed to the free stream (figure 7*e*). Thus, the convergence of F_x^* to unity is much delayed for the other four bristles; in fact, no convergence is observed in the range of $Re_D\,G/D$ considered in figure 7(*e*). Similar to $\alpha = 45°$, the first bristle exhibits the largest F_y^* and F_y^* decreases sequentially from the first bristle to the fifth bristle for $Re_D\,G/D < 3$ (figure 7*f*). The $Re_D\,G/D$ value corresponding to the peak of F_y^* increases slightly from the first to the fourth bristle. The maximum F_y^* is found at $Re_D\,G/D = 1.5$ for the first bristle and at $Re_D\,G/D = 3.0$ for the fourth bristle. The range of $Re_D\,G/D$ corresponding to the maximum lift is wider than for the higher α, i.e. $\alpha = 45°$.

As shown in figure 7, the forces acting on each bristle of the oblique wing model with $\alpha < 90°$ are no longer symmetric with respect to the third bristle in the middle and exhibit different trends from those of the wing model with $\alpha = 90°$. To determine how changing $Re_D\,G/D$ affects the flow fields and the surface force distribution for the oblique wing, we examine the representative case of $\alpha = 45°$ and $Re_D = 0.1$ (figures 8 and 9). Here, we focus on lift because lift can be considered as one of the parameters to determine the aerodynamic performance of the oblique wing and lift changes more notably than drag when we change α from 90° to 45° (figure 7). We choose the two outermost bristles, the first and fifth ones, because they behave differently with regard to lift generation.

For $Re_D\,G/D = 3.0$ close to the maximum lift of the first bristle (figure 7*d*), the y components $f_{p,y}$ and $f_{v,y}$ of the pressure and viscous forces, respectively, change their signs at values of the polar angle θ that are quite different from that of the single isolated bristle, $Re_D\,G/D = \inf.$ (figure 9*a*,*b*). The sign of $f_{p,y}$ changes from positive to negative at $\theta = 108°$ and 286°, and the sign of $f_{v,y}$ changes at $\theta = 18°$ and 196°, thereby helping to enlarge the areas of positive $f_{p,y}$ and $f_{v,y}$ and consequently the overall lift. Interestingly, the polar angle for the change from negative to positive values is unaffected by $Re_D\,G/D$. Moreover, for $Re_D\,G/D = 3.0$ of the first bristle, the magnitudes of the positive peaks of $f_{p,y}$ and $f_{v,y}$ are greater than those of their negative peaks, and a huge deviation from the single isolated bristle is observed for the negative peaks, which also results in enhanced lift. The flow around the first bristle is tilted anticlockwise (figure 8*a*). As mentioned in § 3.1, this tilting corresponds

https://doi.org/10.1017/jfm.2020.64 Published online by Cambridge University Press

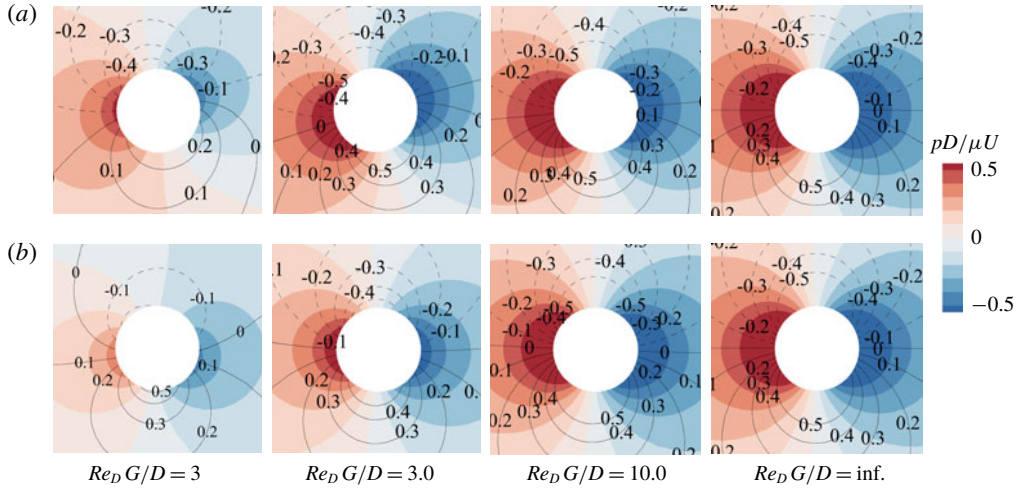


FIGURE 8. Pressure and vorticity contours around (*a*) first bristle and (*b*) fifth bristle of the five-bristle model for $Re_D = 0.1$ and $\alpha = 45°$. The dashed and solid contour lines denote negative and positive vorticities ($\omega D/U$), respectively; and $Re_D\,G/D = \text{inf.}$ indicates the case of a single isolated cylinder.

to lift being produced on the bristle. As expected, the tilting is most notable for $Re_D\,G/D = 3.0$, with the tilting angle defined in § 3.1 being the largest, $\theta_t = 16.7°$.

For $f_{p,y}$ and $f_{v,y}$ of the first bristle, the shift of the polar angle for sign change and the asymmetric distribution of positive and negative peaks are also prominent at $Re_D\,G/D = 0.3$ (figure 9*a*,*b*). In fact, the profiles of $f_{p,y}$ and $f_{v,y}$ for $Re_D\,G/D = 0.3$ differ more from those of a single isolated bristle than do those for $Re_D\,G/D = 3.0$. The tilting angle is $\theta_t = 12.2°$ for $Re_D\,G/D = 0.3$, comparable to $\theta_t = 16.7°$ for $Re_D\,G/D = 3$ (figure 8*a*). However, because of the reduced magnitudes of pressure and vorticity on the surface, the lift for $Re_D\,G/D = 0.3$ is only 0.54 times that for $Re_D\,G/D = 3$. As the effective gap width increases beyond $Re_D\,G/D = 3.0$, the flow fields become more symmetric, and the profiles of $f_{p,y}$ and $f_{v,y}$ are eventually those for a single isolated bristle.

Meanwhile, the tilting angle θ_t of the fifth bristle remains negative although its magnitude is small, namely $\theta_t = -1.0°$ for $Re_D\,G/D = 0.3$ and $\theta_t = -1.5°$ for $Re_D\,G/D = 3.0$ (figure 8*b*). Indeed, because of this negative tilting, the lift is negative in the entire range of $Re_D\,G/D$ (figure 7*d*). For $Re_D\,G/D \geqq 3.0$, the curves of $f_{p,y}$ and $f_{v,y}$ rarely shift and change their signs at polar angles equivalent to those of the single isolated bristle (figure 9*c*,*d*). Only $f_{p,y}$ for $Re_D\,G/D = 0.3$ displays the curve shift near $\theta = 90°$. Furthermore, both the positive and negative peak values of $f_{p,y}$ and $f_{v,y}$ for $Re_D\,G/D \geqq 3.0$ decrease at a nearly uniform rate from those of the single isolated bristle, thereby leading to low lift (figure 7*d*). Although the results for the second, third and fourth bristles are not presented here, the trends for these bristles change gradually from those of the first bristle to those of the fifth.

As expected, in addition to individual bristles, the variation in the total force for the entire five-bristle model is determined by $Re_D\,G/D$. In the range $\alpha = 15°$–$75°$ for the angle of attack, the maximum total lift of the entire wing corresponds to $Re_D\,G/D = 1.5$–3.0, a value that decreases monotonically with a reduction in Re_D (figure 10*a*). However, it is notable that the change in $Re_D\,G/D$ from 1.5 to

https://doi.org/10.1017/jfm.2020.64 Published online by Cambridge University Press

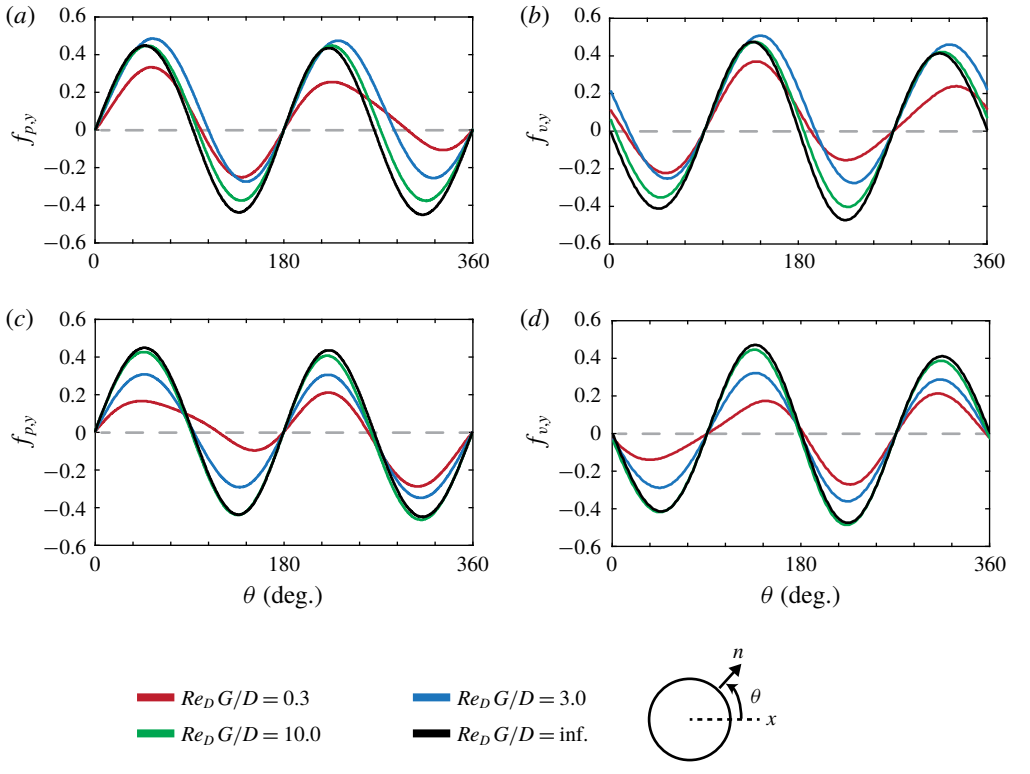


FIGURE 9. Spatial distributions of pressure force and viscous force per unit surface area acting on the surface of (*a*,*b*) first bristle and (*c*,*d*) fifth bristle of the five-bristle model for $Re_D = 0.1$ and $\alpha = 45°$: y component of (*a*,*c*) pressure force and (*b*,*d*) viscous force.

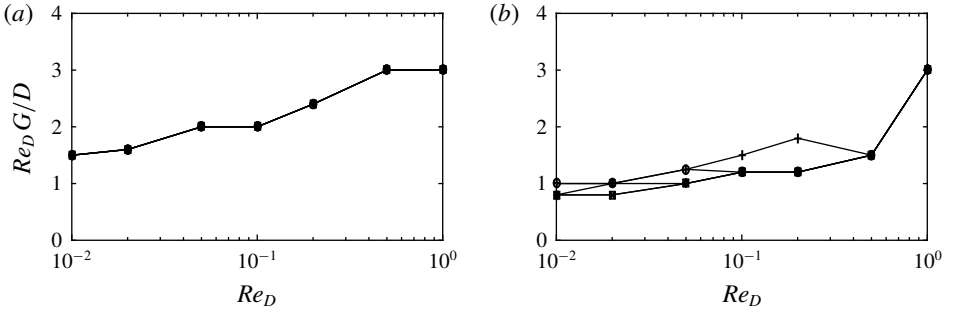


FIGURE 10. Effective gap width $Re_D\,G/D$ that maximizes (*a*) lift and (*b*) lift-to-drag ratio of the entire five-bristle model at a given Re_D. The angle of attack α varies from 15° to 75°: $\alpha = 15°$ (+), 30° (○), 45° (∗), 60° (×) and 75° (□).

3.0 is negligible compared to the 100-fold increment in Re_D from 0.01 to 1. We conjecture that the optimal value of $Re_D\,G/D$ leading to the lift peak will converge asymptotically as Re_D approaches zero. Interestingly, the effective gap width that maximizes the total lift of the entire wing is hardly affected by the change in the angle of attack considered in this study at a given Re_D; the curves for different

https://doi.org/10.1017/jfm.2020.64 Published online by Cambridge University Press

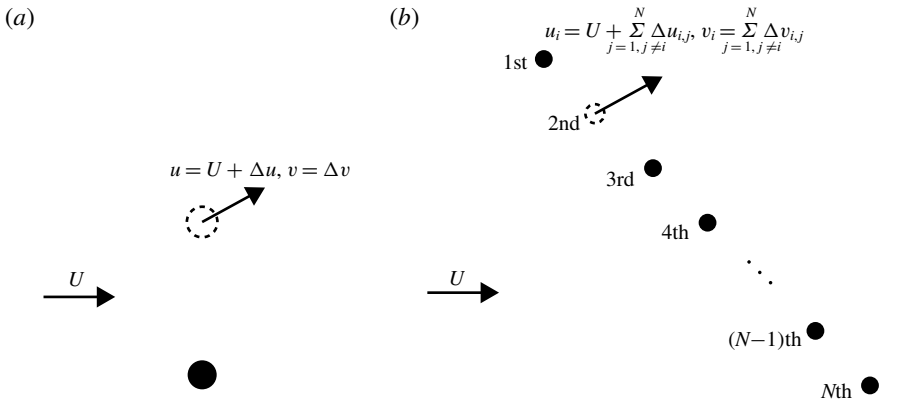


FIGURE 11. Perturbed velocity in (*a*) two-bristle model and (*b*) *N*-bristle model, where *N* is the number of bristles. Here Δu_i and Δv_i are the *x*- and *y*-directional velocity perturbations, respectively, at the centre of the dashed bristle as induced by the other bristles.

angles of attack in figure 10(*a*) are all collapsed. Moreover, the effective gap width that has the maximum lift-to-drag ratio for the entire five-bristle model is also in a narrow range between $Re_D\, G/D = 1.0$ and 3.0 (figure 10*b*). Similar to the lift presented in figure 10(*a*), the effect of the angle of attack on determining optimal $Re_D\, G/D$ for lift-to-drag ratio is insignificant as well, although some variation among different values of α is observed. These intriguing results in figure 10 offer insightful information on how the arrangement of the bristled wing should be adjusted in response to the change in the angle of attack.

3.3. *Force estimation for five-bristle model*

With the effective gap width introduced, we now estimate the lift and drag acting on the five-bristle model by using a simple theoretical approach that is useful for analysing the optimal configuration of a bristled wing. To explain the principle more simply, we begin by supposing that a bristle (solid circle) is placed alone in a uniform free stream of speed U (figure 11*a*). The velocity perturbations induced by this bristle in the x and y directions are Δu and Δv, respectively, giving a perturbed velocity field $u = U + \Delta u$, $v = +\Delta v$. When a new bristle (dashed circle) is introduced at an arbitrary position, the aerodynamic force applied to the new bristle can be estimated by assuming that the new bristle is subjected to the uniform free stream with $u = U + \Delta u$, $v = +\Delta v$ corresponding to its position because of the linearity of the governing equations of low-Reynolds-number flow (Happel & Brenner 1983). This assumption is reasonable except when the distance between the bristles is very small. The limitations of this theoretical approach and an alternative force estimation model for narrow gaps are addressed later in this section.

According to Tomotika & Aoi (1951), the drag force exerted on a single isolated bristle is approximated as

$$F = 4\pi\mu U \Delta(Re_D) = \frac{4\pi\mu U}{[0.5 - \gamma + \ln(8\mu/\rho U D)]}. \tag{3.5}$$

https://doi.org/10.1017/jfm.2020.64 Published online by Cambridge University Press

Then, in the two-bristle model, the x- and y-directional forces F_x and F_y acting on a bristle (dashed circle in figure 11*a*) can be computed from (3.5) as

$$F_x = \frac{4\pi\mu u}{[0.5 - \gamma + \ln(8\mu/\rho\sqrt{u^2+v^2}D)]} \quad \text{and} \quad F_y = \frac{4\pi\mu v}{[0.5 - \gamma + \ln(8\mu/\rho\sqrt{u^2+v^2}D)]}. \tag{3.6a,b}$$

Instead of the free-stream velocity U, the flow velocity at the position of the bristle, namely $u = U + \Delta u$, $v = \Delta v$, is used in (3.6) to calculate F_x and F_y; u and v are obtained from our numerical simulation with a single isolated bristle. The comparisons between the numerical results and theoretically predicted results by (3.6) for the two-bristle model are given in the Appendix.

This theoretical approach used to predict the forces acting on the simple two-bristle model can be extended to the N-bristle model, where N is the total number of bristles: $N = 5$ for the five-bristle model (figure 11*b*). For the five-bristle model, we assume that the perturbed velocity vector at the location of a new ith bristle (dashed circle) can be obtained by summing the velocity perturbations from the other four bristles (solid circles):

$$u_i = U + \sum_{j=1, j\neq i}^{N} \Delta u_{i,j} \quad \text{and} \quad v_i = \sum_{j=1, j\neq i}^{N} \Delta v_{i,j}, \tag{3.7a,b}$$

where $\Delta u_{i,j}$ and $\Delta v_{i,j}$ are the u- and v-velocity perturbations at the location of the ith bristle, which are induced by the jth bristle. To compute $\Delta u_{i,j}$ and $\Delta v_{i,j}$, we assume that the jth bristle is placed solely in a uniform flow. In other words, by acquiring the velocity field around a single isolated bristle, the velocity vector $[u_i, v_i]$ at any bristle location of the multi-bristle model can be constructed by linear superposition. As mentioned before, we obtain the velocity field around a single isolated bristle from our numerical simulation.

With the velocity vector of (3.7), the lift and drag acting on the ith bristle and the entire five-bristle model can be constructed from (3.6) as

$$F_{x,i} = \frac{4\pi\mu u_i}{[0.5 - \gamma + \ln(8\mu/\rho\sqrt{u_i^2+v_i^2}D)]} \quad \text{and} \quad F_{y,i} = \frac{4\pi\mu v_i}{[0.5 - \gamma + \ln(8\mu/\rho\sqrt{u_i^2+v_i^2}D)]}, \tag{3.8a}$$

$$F_{x,tot} = \sum_{i=1}^{N} F_{x,i} \quad \text{and} \quad F_{y,tot} = \sum_{i=1}^{N} F_{y,i}. \tag{3.8b}$$

As representative cases, the total forces evaluated by (3.8*b*) are shown in figure 12 for two cases, $[Re_D, \alpha] = [0.1, 45°]$ and $[0.1, 15°]$. Interestingly, the theoretical estimations of lift and drag forces by (3.8) are in excellent agreement with the numerical results for high $Re_D\, G/D$, and the discrepancy between them becomes more significant at low $Re_D\, G/D$. This is because the aerodynamic coupling between the bristles is more prevalent and simple linear superposition is no longer valid in the range of small $Re_D\, G/D$ (figure 12). Here, we mean proximity in the context of aerodynamic interaction rather than the physical distance G/D; $Re_D\, G/D$ is a more relevant parameter than G/D.

The difference between the theoretical estimate and the numerical result is notable for F_x^* of $\alpha = 15°$ even at large $Re_D\, G/D$ (figure 12*c*). At low angle of attack, the bristles behind the first one are not exposed fully to the free stream. Consequently, the basic assumption used in (3.7) that the x velocity is simply the sum of the free-stream

https://doi.org/10.1017/jfm.2020.64 Published online by Cambridge University Press

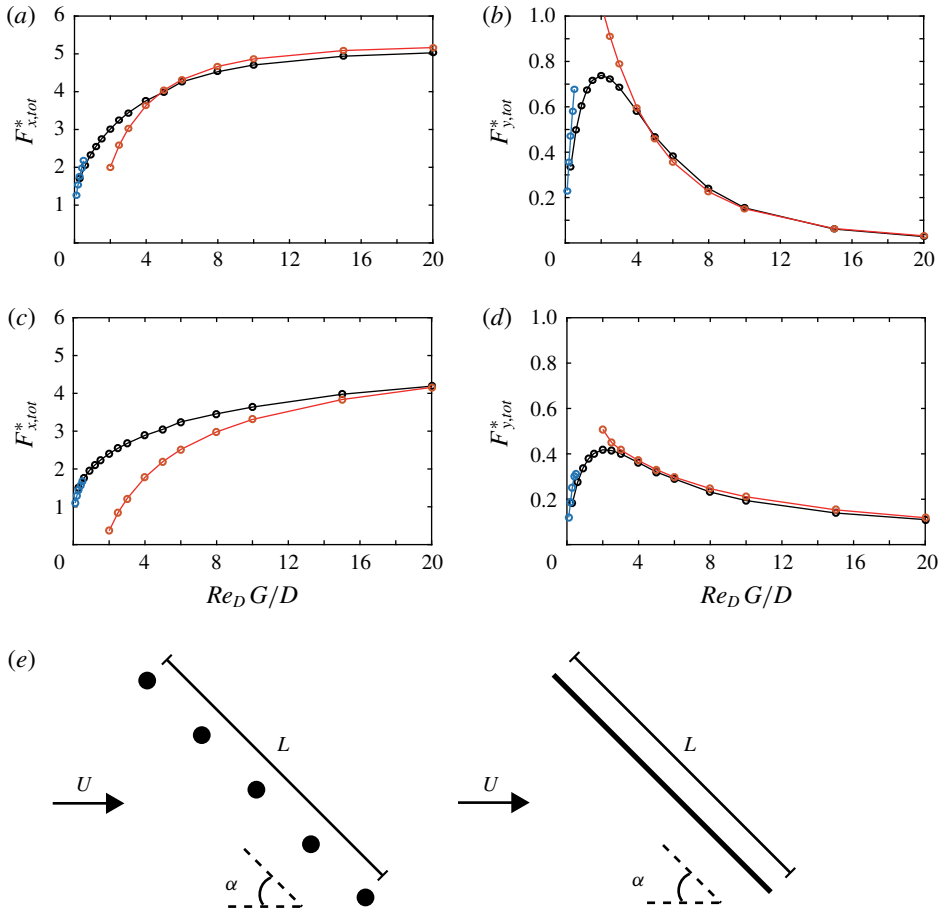


FIGURE 12. Comparison between total drag $F^*_{x,tot}$ and total lift $F^*_{y,tot}$ estimated by (3.8) (red curve) and by the flat-wing model of (3.9) (blue curve) and those obtained by numerical simulation (black curve) for the entire five-bristle model at $Re_D = 0.1$: (*a*,*b*) $\alpha = 45°$; and (*c*,*d*) $\alpha = 15°$. Here $F_{x,tot}$ and $F_{y,tot}$ are normalized by the drag force $F_{x,s}$ of a single isolated bristle with free-stream velocity U. (*e*) Schematic diagrams of a bristled wing and a corresponding flat plate with identical length.

velocity and the perturbed x velocities due to the other bristles is far from acceptable. In contrast to F^*_x, the prediction of (3.8) is quite accurate for F^*_y at large $Re_D\,G/D$ (figure 12*d*), which means that the v-velocity perturbations are less affected by the insufficient exposure to the free stream than are the u-velocity perturbations.

When $Re_D\,G/D$ is small, strong virtual fluid barriers form in the gaps among the bristles to hinder the flow from penetrating the gaps, and the bristle model behaves aerodynamically like a flat wing with no gaps. Therefore, for small $Re_D\,G/D$, we can estimate the force on the five-bristle model by replacing it with a flat plate rather than relying on the inaccurate approach of (3.8) (figure 12*e*). If the Reynolds number is small, the drag and lift coefficients of the flat plate can be expressed analytically (Imai 1954) as

$$C_d = \frac{16\pi}{Re_L}\frac{2S-1-\cos 2\alpha}{G} - \frac{\pi Re_L}{4G}\left[S^2 + \frac{1}{2}(1-2\cos 2\alpha - \cos 4\alpha)S\right.$$

https://doi.org/10.1017/jfm.2020.64 Published online by Cambridge University Press

$$- \frac{1}{24}(9 + 8\cos 2\alpha - 7\cos 4\alpha) + \frac{1}{G}\left(\frac{1}{12}(30 + 23\cos 2\alpha - 10\cos 4\alpha - 3\cos 6\alpha)S - \frac{1}{12}(14 + 21\cos 2\alpha + 6\cos 4\alpha - \cos 6\alpha)\right)\Bigg], \tag{3.9a}$$

$$C_l = \frac{16\pi}{Re_L}\frac{\sin 2\alpha}{G}\left\{1 - \frac{Re_L^2}{64}\left[2S^2 + (1 + \cos 2\alpha)S + \frac{1}{3}(2 - \cos 2\alpha) \times \frac{1}{G}\left(\frac{1}{2}(5 + 4\cos 2\alpha + \cos 4\alpha)S + \frac{1}{3}(9 + 10\cos 2\alpha + \cos 4\alpha)\right)\right]\right\}, \tag{3.9b}$$

where the Reynolds number $Re_L = UL/\nu$ is based on the length of the flat plate, $G = 4S^2 - 2(1 + \cos 2\alpha)$, $S = \ln(16/Re_L) - \gamma$ and $\gamma = 0.5772$ is Euler's constant. If (3.9) is used to predict the forces on the bristled wing at low $Re_D\, G/D$, then L of (3.9) is assumed to be equivalent to the distance between the centres of the first and fifth bristles (figure 12*e*). Then, to acquire $F^*_{x,tot}$ and $F^*_{y,tot}$, the forces $F_{x,tot} = C_d\rho U^2 L/2$ and $F_{y,tot} = C_l\rho U^2 L/2$ on the flat plate are normalized by the drag $F_{x,s}$ on a single isolated bristle of diameter D.

Because (3.9) is applicable to $Re_L < 2$ (Imai 1954), the force obtained by our flat-plate model of (3.9) is valid for $Re_D\, G/D < 0.5$ because $Re_D\, G/D = Re_L/4$. For this reason, we plot the curve in figure 12 for $Re_D\, G/D$ between 0 and 0.5 only. In this $Re_D\, G/D$ range, the forces predicted by the flat-plate model (blue curve) agree well with the actual forces of the five-bristle model (black curve). However, the deviation between them tends to grow with $Re_D\, G/D$. In summary, the flat-plate model (3.9) for small $Re_D\, G/D$ and (3.8) for large $Re_D\, G/D$ suggest good estimation of both drag and lift. In figure 12(*b*) for $F_{y,tot}$ at $\alpha = 45°$, the flat-plate model and (3.8) exhibit the accuracy of predictions within 35 % and 13 % for $Re_D\, G/D < 0.5$ and $Re_D\, G/D > 3.0$, respectively. The accuracies of both models to predict $F_{y,tot}$ improve for $\alpha = 15°$ (figure 12*d*), and the differences are reduced to 22 % and 4 %, respectively. Admittedly, both theoretical models have limited accuracy when estimating the maximum lift, but they allow us to approximate the range of $Re_D\, G/D$ in which maximum lift should arise. In addition to $Re_D = 0.1$, although not reported in figure 12, we confirmed that the aforementioned trends of the forces predicted by the two models pertained also to $Re_D = 0.01$.

Thus far, we have presented $F^*_{x,tot}$ and $F^*_{y,tot}$ of the entire wing as functions of the effective gap width $Re_D\, G/D$. As discussed in § 3.2, the introduction of $Re_D\, G/D$ is motivated by the scaled y coordinate $Re_D\, y/D$ shown in figure 5. According to (3.4), there exists the Reynolds-number-dependent constant $\Delta(Re_D)$ in the leading term of the velocity disturbance. Then, in figure 5, the perturbed velocity is normalized by $\Delta(Re_D)$ to better predict its trend. In a similar way, we provide $F^*_{x,tot}$ and $F^*_{y,tot}$ normalized by $\Delta(Re_D)$ in figure 13(*c*,*d*), namely

$$\frac{F^*_{x,tot} - N}{\Delta(Re_D)}\left(= \sum_{i=1}^{N}\frac{F_{x,i} - F_{x,s}}{F_{x,s}\Delta(Re_D)}\right) \quad \text{and} \quad \frac{F^*_{y,tot}}{\Delta Re_D}. \tag{3.10a,b}$$

While $F^*_{x,tot}$ and $F^*_{y,tot}$ in figure 13(*a*,*b*) show relatively large variations between the curves for different values of Re_D, the curves in figure 13(*c*,*d*) greatly diminish such

https://doi.org/10.1017/jfm.2020.64 Published online by Cambridge University Press

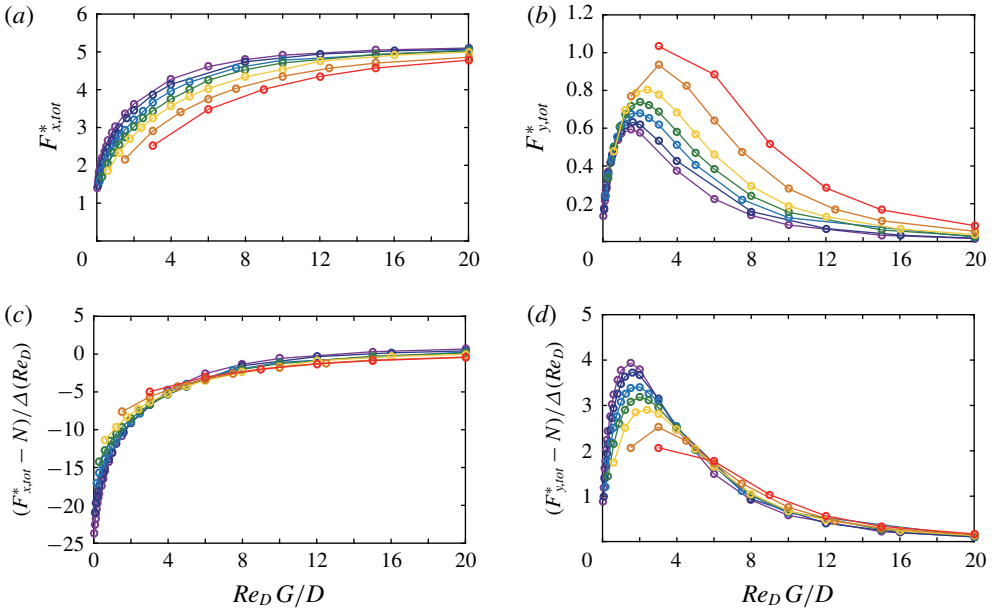


FIGURE 13. (*a*,*b*) Total drag $F^*_{x,tot}$ and total lift $F^*_{y,tot}$ obtained by numerical simulations for the entire five-bristle model at $\alpha = 45°$. (*c*,*d*) Plots of $F^*_{x,tot}$ and $F^*_{y,tot}$ normalized by $\Delta(Re_D) = (\ln(8/Re_D) - \gamma + 0.5)^{-1}$. The plots are for $Re_D = 1$ (red), 0.2 (orange), 0.5 (yellow), 0.1 (green), 0.05 (blue), 0.02 (navy) and 0.01 (purple).

variation and tend to collapse together, in particular for $Re_D\,G/D > 5$. For instance, at $Re_D\,G/D = 6$ and $\alpha = 45°$, $F^*_{y,tot}$ for $Re_D = 1$ is roughly four times greater than that for $Re_D = 0.01$ (figure 13*b*). However, the difference in $F^*_{y,tot}/\Delta(Re_D)$ between $Re_D = 1$ and $Re_D = 0.01$ lies within 20 % under the same conditions (figure 13*d*). The results in figure 13(*c*,*d*) imply that the force normalized by $\Delta(Re_D)$ better characterizes the force trend expressed as a function of $Re_D\,G/D$.

3.4. *Force estimation for 25-bristle model*

The theoretical approaches that we introduced with the five-bristle model can be extended to the model composed of a larger number of bristles. To demonstrate that our findings can be applied generally to a 2-D bristled wing with any number of bristles, a 25-bristle model will be considered here as a representative case. The 25 bristles of diameter D are equally spaced in a straight line (figure 1*b*). For the 25-bristle model, the Reynolds number Re_D ranges from 0.01 to 1.0, i.e. $Re_D = [0.01, 0.02, 0.05, 0.1, 0.2, 0.5, 1.0]$, but the angle of attack, α, is fixed to be 45°.

In a similar way to figure 13, we present $F^*_{x,tot}$ and $F^*_{y,tot}$ of the entire 25-bristle model as functions of the effective gap width $Re_D\,G/D$ (figure 14*a*,*b*). In common with the five-bristle model, the aerodynamic performances are successfully characterized by $Re_D\,G/D$. With $Re_D\,G/D$, the curves of $F^*_{x,tot}$ show a consistent pattern, and converge towards 25 (figure 14*a*). Regardless of the Reynolds number based on D (Re_D), $F^*_{x,tot}$ of each curve is greater than 20 near $Re_D\,G/D > 12$. The total lift has a peak in a narrow range of $Re_D\,G/D$ between 1.5 and 6.0, which is

https://doi.org/10.1017/jfm.2020.64 Published online by Cambridge University Press

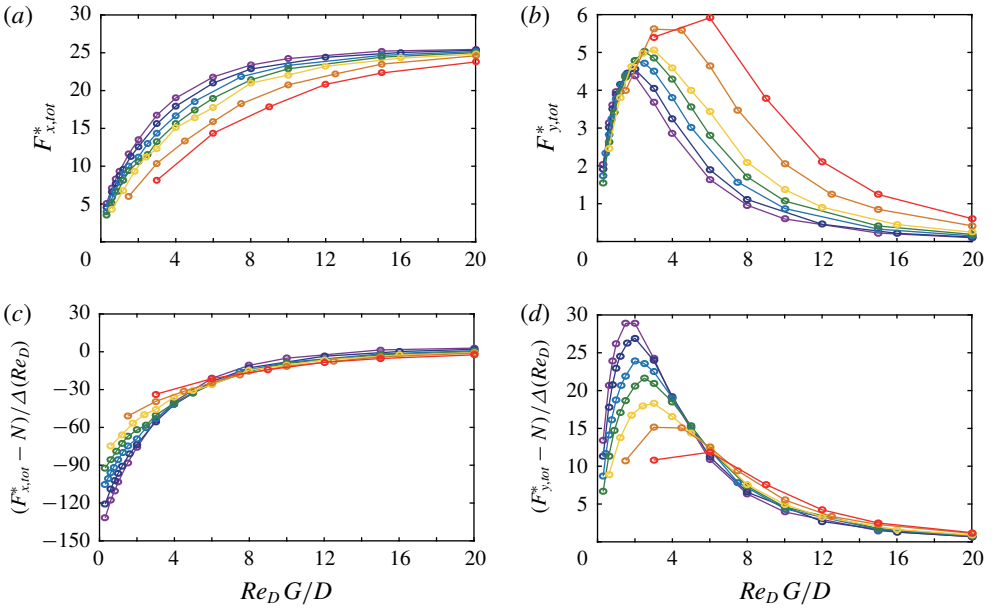


FIGURE 14. (*a*,*b*) Total drag $F^*_{x,tot}$ and total lift $F^*_{y,tot}$ obtained by numerical simulations for the entire 25-bristle model at $\alpha = 45°$. (*c*,*d*) Plots of $F^*_{x,tot}$ and $F^*_{y,tot}$ normalized by $\Delta(Re_D) = (\ln(8/Re_D) - \gamma + 0.5)^{-1}$. The plots are for $Re_D = 1$ (red), 0.2 (orange), 0.5 (yellow), 0.1 (green), 0.05 (blue), 0.02 (navy) and 0.01 (purple).

similar to the five-bristle model (figure 14*b*). Interestingly, the value of $Re_D\,G/D$ corresponding to the peak of the lift is hardly affected by the number of bristles (i.e. five or 25) for Re_D below 0.1. Also, $F^*_{x,tot}$ and $F^*_{y,tot}$ normalized by $\Delta(Re_D)$ are provided for the 25-bristle model (figure 14*c*,*d*); also see (3.10). Similar to the five-bristle model, the deviations between the curves of different Re_D values diminish for $Re_D\,G/D > 6$.

In addition to the characterization of the force trends with $Re_D\,G/D$ and $\Delta(Re_D)$, we will show that the theoretical approach used to predict the forces acting on the five-bristle model (figure 11*b*) can be extended to the 25-bristle model. The perturbed velocity vector at the location of a new ith bristle can be obtained by summing the velocity perturbations from the other 24 bristles as shown in (3.7): $N = 25$. With the velocity components in (3.7), the lift and drag acting on the ith bristle and the entire 25-bristle model can be constructed from (3.8).

The total forces evaluated by (3.8) are shown in figure 15 for one representative case of $Re_D = 0.1$. Similar to the five-bristle model (figure 12), the theoretical estimate of (3.8) matches well with the numerical result for high $Re_D\,G/D$, and the discrepancy between them becomes greater at low $Re_D\,G/D$. For low $Re_D\,G/D$, the simple linear superposition breaks down, and instead the flat-plate model can be considered to estimate the forces. The Reynolds number based on the length of the flat plate, Re_L $(= UL/\nu)$, is much greater than unity even for the smallest $Re_D\,G/D$ $(= 0.3)$ considered in figure 15: $Re_L = 24 Re_D\,G/D \geqslant 7.2$. Therefore, numerically computed forces by In *et al.* (1995) were used for the flat-wing model (blue curves in figure 15). In summary, the flat-plate model for small $Re_D\,G/D$ and (3.8) for large $Re_D\,G/D$ suggest good estimation for both drag and lift. Note that both flat-plate model and

https://doi.org/10.1017/jfm.2020.64 Published online by Cambridge University Press

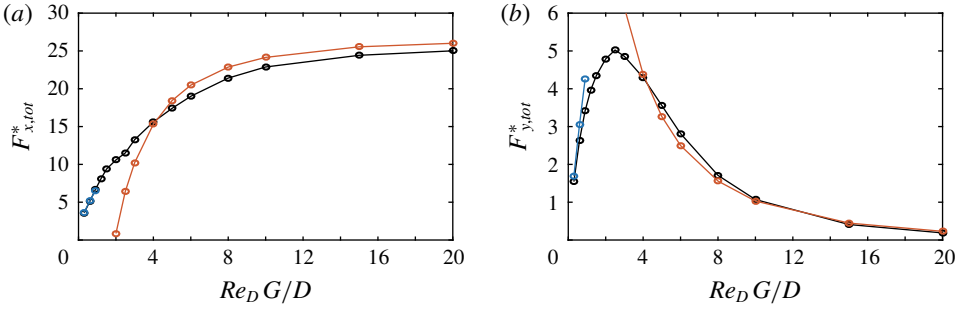


FIGURE 15. Comparison between (*a*) total drag $F^*_{x,tot}$ and (*b*) total lift $F^*_{y,tot}$ estimated by (3.8) (red curve) and by the flat-wing model of In, Choi & Kim (1995) (blue curve) and those obtained by numerical simulation (black curve) for the entire 25-bristle model at $Re_D = 0.1$ and $\alpha = 45°$. Here $F_{x,tot}$ and $F_{y,tot}$ are normalized by the drag force $F_{x,s}$ of a single isolated bristle with free-stream velocity U. The flat-wing model has the same length as the corresponding bristled wing.

(3.8) are valid in almost the same ranges of $Re_D\,G/D$ as those of the five-bristle model (figures 12 and 15). Because of the linear property of the Oseen equation for the flow around the bristled wing, similar trends in force generation are observed regardless of the number of bristles.

4. Concluding remarks

For a bristled-wing model in 2-D low-Reynolds-number flow, we have investigated aerodynamic force generation and its correlation with flow fields in wide ranges of the Reynolds number ($Re_D = 0.01$–1) and gap width ($G/D = 3$–2000). By noting that the Reynolds number and gap width have similar effects on the formation of virtual fluid barriers and the variations of the drag and lift forces exerted on the wing, the effective gap width $Re_D\,G/D$ that couples the Reynolds number and the gap width aerodynamically is introduced to characterize the collective interaction of multiple bristles in low-Reynolds-number flow. As the Reynolds number decreases below $Re_D = 1$, the aerodynamic characterization by the effective gap width $Re_D\,G/D$ is better suited because the flow asymptotically converges to the very-low-Reynolds number solution, where the Reynolds number based on G ($Re_G = Re_D\,G/D$) is the governing parameter. In addition, the scaled force ratio that explicitly includes the Reynolds number is introduced as a new measure of aerodynamic performance. For the five-bristle model, for all Reynolds numbers considered, the total drag normalized by $\Delta(Re_D) = (\ln(8/Re_D) - \gamma + 0.5)^{-1}$ acting on the entire model increases with the effective gap width and converges near $Re_D\,G/D = 6$, and the total lift normalized by $\Delta(Re_D) = (\ln(8/Re_D) - \gamma + 0.5)^{-1}$ has a peak in a narrow range of $Re_D\,G/D$ between 1.5 and 3. The notable trends of the forces in terms of the effective gap width are accounted for by the asymmetric spatial distribution of the forces induced by pressure and viscous stress on the surface of each bristle and the tilting of the pressure and vorticity fields around each bristle.

The drag and lift forces can be predicted theoretically with good accuracy by using the linear superposition of velocity vectors around a single isolated bristle for large $Re_D\,G/D$ and by adopting the alternative flat-plate model for small $Re_D\,G/D$. By virtue of the linearity of the governing equations of low-Reynolds-number flow, we

https://doi.org/10.1017/jfm.2020.64 Published online by Cambridge University Press

can extend the same theoretical approaches for the five-bristle model to the model with the larger number of bristles (e.g. 25-bristle model).

As a fundamental study to obtain insights into how to optimize a bristled wing, our intention herein was to limit our target model to a simple wing with equally spaced identical bristles in a straight line in a 2-D fluid domain instead of considering the actual bristled-wing designs of the smallest insects. Based on the findings and analytical approaches of the present study, in future work we will extend our study to explore the strategies of aerodynamic optimization for more complex configurations such as unequally spaced bristles, cambered bristled wings and ultimately 3-D bristled wings.

Acknowledgements

This research was supported by the Basic Science Research Program through the National Research Foundation of Korea (NRF) funded by the Ministry of Science and ICT (NRF-2017R1E1A1A01074704), and by a grant (KCG-01-2016-04) through the Korea Institute of Marine Science and Technology funded by Korea Coast Guard of Korea government.

Declaration of interests

The authors report no conflict of interest.

Appendix. Two-bristle model

Through § 3, we discussed our results for five- and 25-bristle models. The two-bristle model is the simplest model to confirm whether the characteristics of the creeping flow around a single isolated bristle can be extended to multi-bristle configurations. In fact, before obtaining the results for five- and 25-bristle models, we preliminarily examined the two-bristle model in which two bristles are arranged side-by-side, normal to the free stream ($\alpha = 90°$). The results for the two-bristle model are briefly presented in figure 16.

The drag F_x^* and lift F_y^* forces on the upper bristle of the two-bristle model are better characterized by the effective gap width $Re_D\, G/D$, rather than by the gap width ratio G/D (figure 16*a–d*), similar to the five- and 25-bristle models (figures 13*a*,*b* and 14*a*,*b*). The F_x^* value converges near $Re_D\, G/D = 6$, and F_y^* has a peak in a narrow range of $Re_D\, G/D$ around 3. In addition, F_x^* and F_y^* normalized by $\Delta(Re_D)$ collapse together regardless of the values of Re_D (figure 16*e*,*f*). The same trend is reported for the five- and 25-bristle models with minor variation between curves around $Re_D\, G/D < 5$ (figures 13*a*,*b* and 14*a*,*b*).

The numerical results and theoretically predicted results for the two-bristle model at $\alpha = 90°$ are compared in figure 17. As discussed in §§ 3.3 and 3.4, the forces theoretically estimated by (3.8) are in excellent agreement with the numerically calculated forces for the large effective gap width $Re_D\, G/D$ (figure 17). The assumption used to derive (3.8) is not valid when the bristles are very close to each other, because the perturbation induced by a bristle becomes significant. Indeed, for small $Re_D\, G/D$, relatively large discrepancy is observed between the theoretical prediction and the numerical result. The difference in F_x^* becomes notable at $Re_D\, G/D < 1$. Meanwhile, F_y^* shows greater discrepancy than does F_x^* in the broader range of $Re_D\, G/D$, and the peak of F_y^* presents an error of roughly 20 % from the numerical result. Given that the magnitude of F_y^* is one order smaller than that of

https://doi.org/10.1017/jfm.2020.64 Published online by Cambridge University Press

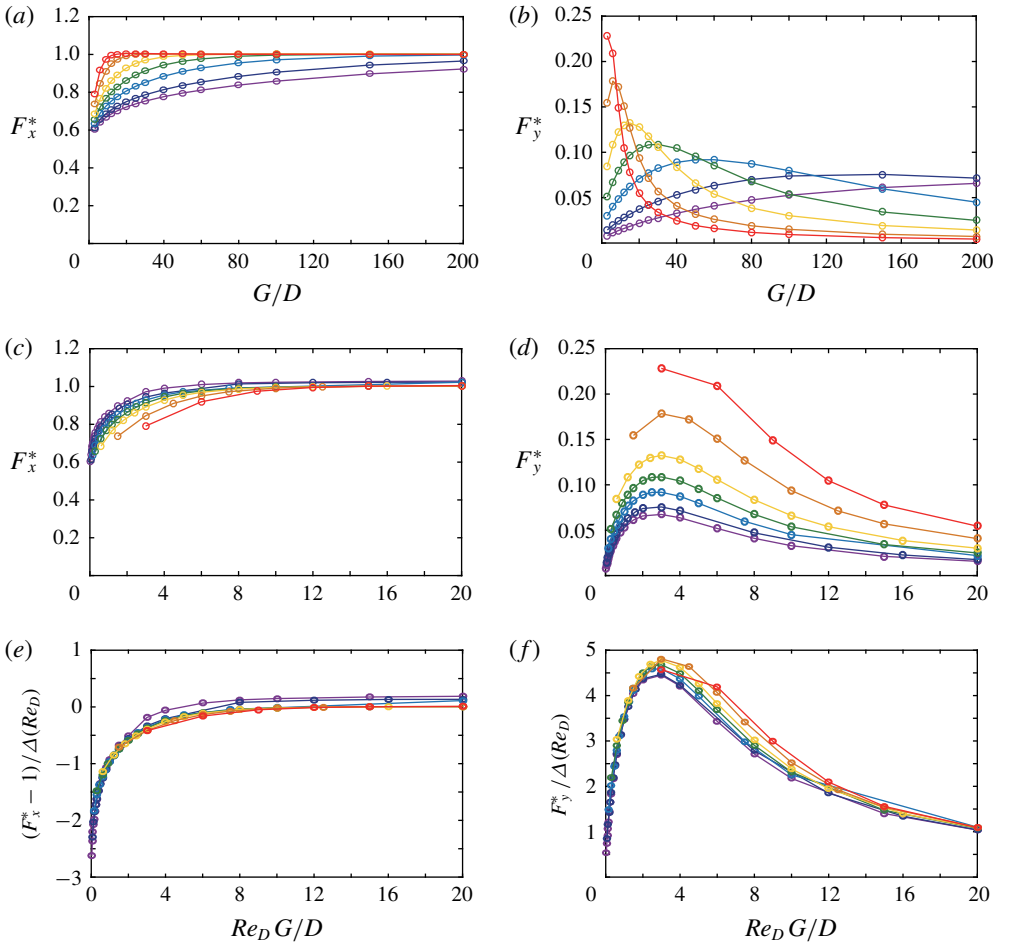


FIGURE 16. (*a*,*b*) Drag F_x^* and lift F_y^* forces of the upper bristle in two-bristle model at $\alpha = 90°$; (*c*,*d*) F_x^* and F_y^* replotted with effective gap width $Re_D\,G/D$; and (*e*,*f*) F_x^* and F_y^* normalized by $\Delta(Re_D) = (\ln(8/Re_D) - \gamma + 0.5)^{-1}$. The plots are for $Re_D = 1$ (red), 0.2 (orange), 0.5 (yellow), 0.1 (green), 0.05 (blue), 0.02 (navy) and 0.01 (purple).

F_x^* in figure 17, note that the prediction of F_y^* is also good if the order of magnitude is considered.

The numerical results and theoretically predicted results in figure 17 show the better agreement for $Re_D = 0.01$, compared to $Re_D = 0.1$, because of the stronger linearity of the flow field and force. For both $Re_D = 0.1$ and 0.01, the drag curves of the numerical simulation and theoretical prediction begin to differ as $Re_D\,G/D$ approaches zero. However, a notable discrepancy begins to occur at smaller $Re_D\,G/D$ for $Re_D = 0.01$, compared to $Re_D = 0.1$ (figure 17*a*,*c*). At $Re_D\,G/D = 0.3$, for example, the numerically computed value of F_x^* is 1.50 times greater than that of the theoretically predicted value for $Re_D = 0.1$. Meanwhile, for $Re_D = 0.01$, the numerical value of F_x^* is only 1.15 times the theoretical value. Similar trends are also observed in the curves of F_y^* (figure 17*b*,*d*).

https://doi.org/10.1017/jfm.2020.64 Published online by Cambridge University Press

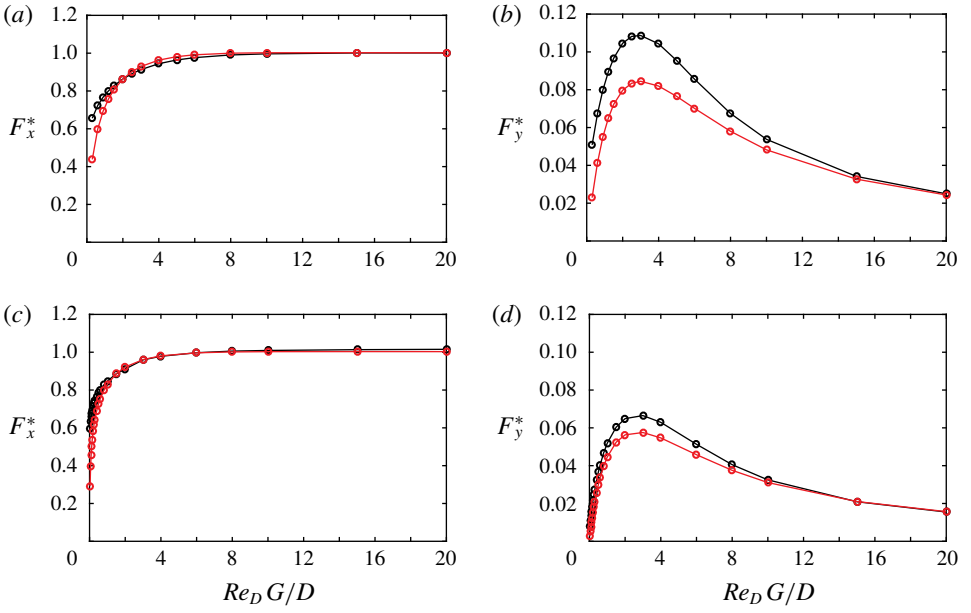


FIGURE 17. Comparison between drag and lift forces estimated by (3.6) (red curve) and those obtained by numerical simulation (black curve) for the upper bristle of the two-bristle model at $\alpha = 90°$: (*a*,*b*) $Re_D = 0.1$; and (*c*,*d*) $Re_D = 0.01$. The forces are normalized by the drag force $F_{x,s}$ of a single isolated bristle with free-stream velocity U; see (3.1).

REFERENCES

BARTA, E. 2011 Motion of slender bodies in unsteady Stokes flow. *J. Fluid Mech.* **688**, 66–87.

BARTA, E. & WEIHS, D. 2006 Creeping flow around a finite row of slender bodies in close proximity. *J. Fluid Mech.* **551**, 1–17.

CHEER, A. Y. L. & KOEHL, M. A. R. 1987 Paddles and rakes: fluid flow through bristles appendages of small organisms. *J. Theor. Biol.* **129**, 17–39.

CUMMINS, C., SEALE, M., MACENTE, A., CERTINI, D., MASTROPAOLO, E., VIOLA, I. M. & NAKAYAMA, N. 2018 A separated vortex ring underlies the flight of the dandelion. *Nature* **562** (7727), 414–418.

DAVIDI, G. & WEIHS, D. 2012 Flow around a comb wing in low-Reynolds-number flow. *AIAA J.* **50**, 249–253.

DICKINSON, M. H., LEHMANN, F.-O. & SANE, S. P. 1999 Wing rotation and the aerodynamic basis of insect flight. *Science* **284**, 1954–1960.

ELLINGTON, C. P., VAN DEN BERG, C., WILLMOTT, A. P. & THOMAS, A. L. R. 1996 Leading-edge vortices in insect flight. *Nature* **384**, 626–630.

GEORGE, P. JR & HUBER, J. T. 2011 A new genus of fossil Mymaridae (Hymenoptera) from Cretaceous amber and key to Cretaceous mymarid genera. *Zookeys* **130**, 461–472.

HAPPEL, J. & BRENNER, H. 1983 *Low Reynolds Number Hydrodynamics*. Martin Nijhoff.

HUBER, J. T. & NOYES, J. S. 2013 A new genus and species of fairyfly, *Tinkerbella nana* (Hymenoptera, Mymaridae), with comments on its sister genus *Kikiki*, and discussion on small size limits in arthropods. *J. Hymenopt. Res.* **32**, 17–44.

IMAI, I. 1954 A new method of solving Oseen's equations and its application to the flow past an inclined elliptic cylinder. *Proc. R. Soc. Lond.* A **224**, 141–160.

IN, K. M., CHOI, D. H. & KIM, M. U. 1995 Two-dimensional viscous flow past a flat plate. *Fluid Dyn. Res.* **15**, 13–24.

https://doi.org/10.1017/jfm.2020.64 Published online by Cambridge University Press

JONES, S. K., YUN, Y. J. J., HEDRICK, T. L., GRIFFITH, B. E. & MILLER, L. A. 2016 Bristles reduce the force required to 'fling' wings apart in the smallest insects. *J. Expl Biol.* **219**, 3759–3772.

KASOJU, V. T., TERRILL, C. L., FORD, M. P. & SANTHANAKRISHNAN, A. 2018 Leaky flow through simplified physical models of bristled wings of tiny insects during clap and fling. *Fluids* **3**, 44.

KHALILI, A. & LIU, B. 2017 Stokes' paradox: creeping flow past a two-dimensional cylinder in an infinite domain. *J. Fluid Mech.* **817**, 374–387.

KIM, D., LEE, S. H. & KIM, D. 2019 Aerodynamic interaction of collective plates in side-by-side arrangement. *Phys. Fluids* **31**, 071902.

KOEHL, M. A. R. 1996 Small scale fluid dynamics of olfactory antennae. *Mar. Freshw. Behav. Physiol.* **27**, 127–141.

KOEHL, M. A. R., KOSEFF, J. R., CRIMALDI, J. P., MCCAY, M. G., COOPER, T., WILEY, M. B. & MOORE, P. A. 2001 Lobster sniffing: antennule design and hydrodynamic filtering of information in an odor plume. *Science* **294**, 1948–1951.

LEE, S. H. & KIM, D. 2017 Aerodynamics of a translating comb-like plate inspired by a fairyfly wing. *Phys. Fluids* **29**, 081902.

LEE, S. H., LAHOOTI, M. & KIM, D. 2018 Aerodynamic characteristics of unsteady gap flow in a bristled wing. *Phys. Fluids* **30**, 071901.

LEE, S. H. & LEAL, L. G. 1986 Low-Reynolds-number flow past cylindrical bodies of arbitrary cross-sectional shape. *J. Fluid Mech.* **164**, 401–427.

NAWROTH, J. C., FEITL, K. E., COLIN, S. P., COSTELLO, J. H. & DABIRI, J. O. 2010 Phenotypic plasticity in juvenile jellyfish medusae facilitates effective animal-fluid interaction. *Biol. Lett.* **6**, 389–393.

PROUDMAN, I. & PEARSON, J. R. A. 1957 Expansions at small Reynolds numbers for the flow past a sphere and a circular cylinder. *J. Fluid Mech.* **2**, 237–262.

SANTHANAKRISHNAN, A., ROBINSON, A. K., JONES, S., LOWE, A., GADI, S., HEDRICK, T. L. & MILLER, L. A. 2014 Clap and fling mechanism with interacting porous wings in tiny insect flight. *J. Expl Biol.* **217**, 3898–3909.

SUNADA, S., TAKASHIMA, H., HATTORI, T., YASUDA, K. & KAWACHI, K. 2002 Fluid-dynamic characteristics of a bristled wing. *J. Expl Biol.* **205**, 2737–2744.

TOMOTIKA, S. & AOI, T. 1951 An expansion formula for the drag on a circular cylinder moving through a viscous fluid at small Reynolds numbers. *Q. J. Mech. Appl. Maths* **4**, 401–406.

UMEMURA, A. 1982 Matched-asymptotic analysis of low-Reynolds-number flow past two equal circular cylinders. *J. Fluid Mech.* **328**, 345–407.

VAN DYKE, M. 1975 *Perturbation Methods in Fluid Mechanics*. Parabolic.

WEIHS, D. & BARTA, E. 2008 Comb wings for flapping flight at extremely low Reynolds numbers. *AIAA J.* **46**, 285–288.

WEIS-FOGH, T. 1973 Quick estimates of flight fitness in hovering animals, including novel mechanisms for lift production. *J. Expl Biol.* **59**, 169–230.

ZUSSMAN, E., YARIN, A. L. & WEIHS, D. 2002 A micro-aerodynamic decelerator based on permeable surfaces of nanofiber mats. *Exp. Fluids* **33**, 315–320.

https://doi.org/10.1017/jfm.2020.64 Published online by Cambridge University Press